



HAL
open science

Operando Surface X-ray Diffraction Studies of Structurally Defined Co_3O_4 and CoOOH Thin Films during Oxygen Evolution

Finn Reikowski, Fouad Maroun, Ivan Pacheco, Tim Wiegmann, Philippe Allongue, Jochim Stettner, Olaf Magnussen

► **To cite this version:**

Finn Reikowski, Fouad Maroun, Ivan Pacheco, Tim Wiegmann, Philippe Allongue, et al.. Operando Surface X-ray Diffraction Studies of Structurally Defined Co_3O_4 and CoOOH Thin Films during Oxygen Evolution. ACS Catalysis, 2019, 9 (5), pp.3811-3821. 10.1021/acscatal.8b04823. hal-02324891

HAL Id: hal-02324891

<https://hal.science/hal-02324891>

Submitted on 23 Aug 2021

HAL is a multi-disciplinary open access archive for the deposit and dissemination of scientific research documents, whether they are published or not. The documents may come from teaching and research institutions in France or abroad, or from public or private research centers.

L'archive ouverte pluridisciplinaire **HAL**, est destinée au dépôt et à la diffusion de documents scientifiques de niveau recherche, publiés ou non, émanant des établissements d'enseignement et de recherche français ou étrangers, des laboratoires publics ou privés.

***Operando* Surface X-ray Diffraction Studies of Structurally-defined Co_3O_4 and CoOOH Thin Films during Oxygen Evolution**

Finn Reikowski,¹ Fouad Maroun,² Ivan Pacheco,² Tim Wiegmann¹

Philippe Allongue^{2*}, Jochim Stettner,¹ and Olaf M. Magnussen^{1*}

¹ Institute of Experimental and Applied Physics, Kiel University, 24098 Kiel, Germany

² Physique de la Matière Condensée, Ecole Polytechnique, CNRS, 91128 Palaiseau, France

*Corresponding authors: philippe.allongue@polytechnique.edu; magnussen@physik.uni-kiel.de

Abstract

In the search for precious-metal free electrode materials for electrochemical water splitting, transition metal oxides have been receiving much recent interest as active and stable electrocatalysts for the anodic oxygen evolution reaction (OER). We present *operando* surface X-ray diffraction studies of two structurally well-defined epitaxial cobalt oxide thin films – $\text{Co}_3\text{O}_4(111)$ and $\text{CoOOH}(001)$ electrodeposited on $\text{Au}(111)$. The potential-dependent structural changes during cyclic voltammograms were monitored with high time resolution up to OER current densities as high as 150 mA cm^{-2} . The $\text{CoOOH}(001)$ film is found to be smooth and perfectly stable over a wide potential range. In the case of $\text{Co}_3\text{O}_4(111)$, fast and fully reversible structural changes are observed. Specifically, the surface region of $\text{Co}_3\text{O}_4(111)$ starts restructuring at potentials 300 mV negative of the onset of the OER, indicating that the process is related to the thermodynamically predicted $\text{Co}_3\text{O}_4 / \text{CoOOH}(001)$ transition rather than to the catalytic reaction. The formed skin layer is of defined thickness, which changes linearly with applied potential, and is the OER active phase. Surprisingly, the catalytic activity of the skin layer covered Co_3O_4 film and that of the smooth $\text{CoOOH}(001)$ are almost identical, if the true microscopic surface area is taken into account.

This indicates that the number of OER active sites on the two oxides is similar, despite the very different defect density, and is at variance with previous suggestions that di- μ -oxo bridged Co cations are exclusively responsible for the OER activity of Co oxides. For the smooth CoOOH(001) a turnover frequency of 4.2 s^{-1} per surface atom is determined at an overpotential of 400 mV. Furthermore, our studies demonstrate that the pseudo-capacitive charging current in the pre-OER potential range must be assigned to a bulk process that is accompanied by potential-dependent changes of the unit cell volume in the Co_3O_4 bulk.

Keywords:

oxygen evolution reaction, electrocatalysts, Co_3O_4 , CoOOH, operando studies, surface X-ray diffraction

1. Introduction

The need for environmental friendly and sustainable energy conversion, which allows scalable storage of wind and solar electricity into fuels, has triggered renewed interest into the electrochemical and photoelectrochemical splitting of water.¹ A key challenge in this field is the development of economically viable electrocatalyst materials for the oxygen evolution reaction (OER). Transition metal oxides catalysts, in particular the different cobalt (hydr)oxide phases, have received large attention because they meet these requirements.^{2 3 4} These materials are earth abundant, easy to prepare, and present good catalytic properties and stability in alkaline and neutral electrolytes.^{2,5,6,7} Cobalt oxides may be prepared with an amorphous or a crystalline structure, using a variety of methods, including thermal salt decomposition,⁸ autoclave synthesis,⁹ photochemical reactions,¹⁰ sol-gel synthesis,¹¹ Co electrodeposition and subsequent oxidation,^{12,13,14} and direct oxide electrodeposition.^{2,15,16}

For understanding and further developing Co oxide catalysts it is necessary to clearly separate intrinsic structure-property relationships, which describe the dependence of the OER activity on the atomic-scale surface structure, from effects caused by the nano- and microscale material morphology. It was suggested that in comparing different catalysts, benchmarking protocols should be followed to determine at a defined overpotential the OER turn over frequency (TOF)– the average number of O₂ molecules formed per unit of time and per catalytic site.^{17,18} For this, the electrochemical surface area (ECSA) has to be measured, which is not trivial for these materials.^{5,18} As a further complication, often pre-conditioning of the catalyst is reported to be necessary for a stable OER current-potential characteristic. In general, an improved characteristic is obtained,¹⁹ which suggests a significant restructuring of the catalyst surface under reaction conditions. Such transformations were, for instance, evidenced in the case of nanocrystalline Co₃O₄, for which OER was reported to induce conversion of a nanometer thick surface region into another phase with a higher Co oxidation

state and modified local arrangement.^{11,19,20,21} Ideally, the density and atomic configuration of the active sites should therefore be determined *operando* during oxygen evolution.

The mechanisms of the OER on cobalt oxides has been investigated in great detail.^{18,22} On the molecular scale, it is a complex four-step reaction which generally is proposed to start with bulk water nucleophilic attack, i.e., the formation of an O-O bond after a water molecule has reacted with a terminal or bridging oxygen. This process implies a nominal increase of the oxidation state of surface atoms to $\text{Co}^{3+/4+}$. Indication for the latter was found by *operando* X-ray adsorption spectroscopy (XAS)^{11,14,19,23,24} and near-ambient-pressure X-ray photoelectron spectroscopy (XPS).^{21,25} The O_2 formation involves the participation of oxygen from the oxide lattice, as inferred from differential electrochemical mass spectroscopy (DEMS) measurements, conducted with samples prepared in H_2^{18}O labelled water^{26,27} and with samples immersed in electrolytes prepared with labelled water.²⁷ Formation of superoxide/oxo intermediates at dicobalt sites, which were identified with step edge sites, was also observed by time resolved IR spectroscopy.^{28,29}

On the atomic scale, Dau et al.³⁰ concluded on the basis of X-ray absorption spectroscopy (XAS) studies of electrodeposited amorphous Co oxide films (frequently referred to as CoCat) that the film consists of small clusters of Co-oxo cubanes, in which the oxygen atoms are coordinated to two neighbouring Co ions ($\mu_2\text{-O}$), and that this configuration corresponds to the catalytically active sites. This conclusion was supported by density functional theory (DFT) calculations, which predicted that CoOOH is the active phase during OER and discussed the stability of the surface orientation.^{31,32} Further support came from experiments with molecular Co compounds that are mimicking these sites.^{26,33} Because the amorphous CoCat films exhibit excellent OER catalytic activity,^{2, 34} it is now widely accepted that this motif is the most catalytically active sites on any cobalt oxide sample.^{26,18,19,29,35} Nevertheless,

direct evidence that the OER activity of μ_2 -O is superior to other Co sites has not been reported so far.

A key problem in the unambiguous identification of the active sites is the complex (typically polycrystalline or amorphous) structure and morphology of the studied Co oxide samples. A number of studies have attempted to address this by employing catalyst materials with preferred surface orientations, such as shaped Co_3O_4 nanoparticles^{12, 20, 36} and exfoliated CoOOH nanosheets.^{37,38} While these studies indicated an effect of the surface structure, measuring the ECSA remained a problem with these samples. For obtaining clear structure-reactivity correlations, structurally well-defined model OER catalysts are necessary. Such model catalysts may be single crystals or epitaxial layers of defined morphology, for which the atomic structure and density of surface sites can be precisely determined. While this is a well-established approach in heterogeneous catalysis and in electrocatalysis on metal electrode surfaces, OER studies with cobalt oxide model catalysts remain the exception. An exemplary study employing this strategy was recently published by Libuda and co-workers.³⁹ Here, ultrathin Co_3O_4 (111) epitaxial layer were grown by physical vapor deposition on $\text{Ir}(001)$, characterized *ex situ* under ultrahigh vacuum (UHV) conditions, and transferred without exposure to air into an electrochemical cell for cyclic voltammetry (CV) and differential electrochemical mass spectroscopy studies.

In this work, we apply a similar approach, but combine the use of epitaxial Co oxide films with an *operando* structural characterization of cobalt oxide model catalysts by surface X-ray diffraction (SXRD) during the electrochemical measurements. The Co oxide samples were prepared by electrodeposition of nanometer thick films on $\text{Au}(111)$ single crystal electrodes, using a method adapted from that published by Switzer and co-workers.^{12,16} SXRD and complementary atomic force microscopy (AFM) measurements show that well-defined epitaxial $\text{Co}_3\text{O}_4(111)$ and $\text{CoOOH}(001)$ oxide films are obtained. The *operando* SXRD

studies reveal remarkable differences in the potential-dependent surface structure of the two oxide surfaces, whereas their catalytic properties appear very similar. We discuss the implications of these results on the origin of the structural transformation of the near-surface layer of Co_3O_4 , the nature of the OER-active sites, and the pseudo-capacitive charging / discharging of cobalt oxide in the pre-OER region.

2. Experimental

Thin films of cobalt oxides were electrodeposited on Au(111) substrates using a procedure adapted from that developed by Switzer and co-workers.¹⁶ The method consists in electrooxidizing at 1 V_{RHE} at reflux temperature ($\sim 103^\circ\text{C}$) a diluted oxygen-free solution of 1 mM $\text{Co}(\text{NO}_3)_2$ + 1.2 mM sodium tartrate (tart) in 2 or 5 M NaOH, prepared from high purity Co nitrate (Merck, > 99.0%), Na tartrate (Sigma Aldrich, ACS reagent > 99.5%), NaOH (Merck, ACS reagent, Fe content < 0.00005%), and Milli-Q water. A charge of 8 mC was passed to grow films with 15-25 nm thickness. The substrate was a hat-shaped Au(111) single crystal (MaTeck) with an orientation uncertainty of < 0.1° . Prior to oxide film preparation, the Au crystals were immersed in a hot 1:2 mixture of 30% H_2O_2 and 96% H_2SO_4 (both Carlo Erba, RSE) for 1 minute to remove any remaining oxide from previous experiments and then annealed in a butane flame for 5 minutes. After deposition, the samples were quickly removed from the reflux cell, rinsed with ultrapure water, dried with Ar, and inserted into the SXR cell.

Operando SXR studies were conducted at ESRF Beam line ID 03, at a photon energy of 22.5 keV with a flux of 4×10^{11} counts/s and a beam of 250 μm in width and 30 μm in height. Measurements were performed in six-circle geometry, using a fixed incident angle of 0.34° (see Figure S1). The footprint of the beam on the sample was 250 $\mu\text{m} \times 5$ mm. It is convenient in SXR on (111) surfaces of fcc metal substrates⁴⁰ to employ a hexagonal

reciprocal space geometry, where q_z is along the surface normal and q_x , q_y are oriented perpendicular to the main in-plane lattice directions (see Figure 1c). Here, the reciprocal space positions (H, K, L) are given in units of the lattice vectors $a^* = \frac{4\pi}{\sqrt{3}a_{nn}} = 2.51 \text{ \AA}^{-1}$ and $c^* = \frac{2\pi}{\sqrt{6}a_{nn}} = 0.89 \text{ \AA}^{-1}$ with $a_{nn} = 2.885 \text{ \AA}$ being the Au nearest neighbour spacing. However, the indices of the Bragg peaks of the studied Co_3O_4 and CoOOH films refers to the conventional simple cubic and hexagonal unit cells of these materials, respectively, to ease comparison with the literature.

During the measurements, the cylindrical sample was kept in a specifically designed electrochemical cell for SXRD studies, made from PEEK, and embedded in a teflon seal. This way, only the polished Au(111) top part of the sample (geometric area 0.125 cm^2), on which the epitaxial film had been deposited, was exposed to the electrolyte. Potential control was established using a glassy carbon rod as counter electrode and a Ag/AgCl reference electrode. All potentials are referred to the reversible hydrogen electrode (RHE) to ease comparison with literature and are IR corrected. The electrolyte consists of 0.1 M NaOH, made from suprapure NaOH (Aldrich) and Milli-Q water, and was continuously exchanged via computer controlled syringes at a rate of 5-20 $\mu\text{L/s}$ to avoid accumulation of species (radicals) generated by the X-ray beam as well as minimize O_2 bubble formation and transport limitations.

3. Results

3.1 Structure of as prepared epitaxial Co oxide films

The SXRD studies show that structurally well-defined Co oxide films can be prepared by the employed electrodeposition procedure. Their structure is determined from the measured diffraction intensities in reciprocal space. Examples of such measurements, obtained on the as-prepared films in the SXRD cell under argon atmosphere, are shown for films deposited in 2 M (Figure 1a) and 5 M (Figure 1b) NaOH solution. Scans along the (0, 1, L) crystal

truncation rods of the Au substrate reveal additional Bragg peaks, which can be assigned to crystalline (hydr)oxide phases (Figure 1a,b), specifically Co_3O_4 and CoOOH . The first oxide is a spinel with a face centred cubic unit cell,⁴¹ the second has a hexagonal structure (called Heterogenite-3R⁴² or β - CoOOH ^{4,14,31}, JCPDS card 07-0169).

As illustrated by the schematic reciprocal space geometry in Figure 1c, the peak positions along these and other (not shown) truncation rods coincide with those expected for a (111)-oriented Co_3O_4 film (red lines, Figure 1a) and a (001)-oriented film of CoOOH (blue lines, Figure 1b). The measured lattice parameters of the former agree well with the literature value (red lines in Figure 1a), the CoOOH lattice is expanded by $\approx 1\%$, adopting the Au substrate lattice spacing within the surface plane. Complementary in-plane characterizations confirm that the lattices of the deposits exhibit a sixfold symmetry with respect to the surface normal, where the main in-plane directions (e.g. $\text{Co}_3\text{O}_4[044]$ and $\text{CoOOH}[100]$) are aligned to the main in-plane axes of the Au surface (i.e., H or K). The in-plane angular spread of the crystallites is $\approx 1^\circ$ for Co_3O_4 and below the detection limit for CoOOH . For the shown samples, no other Co oxide phases or orientations are found, i.e. the deposits are pure phases and in excellent epitaxy with the Au(111) substrate. Proof of the latter is also that Bragg peaks, which are located along other CTRs (e.g., the $\text{Co}_3\text{O}_4(333)$ or the $\text{Co}_3\text{O}_4(422)$ peak), are not observed in the (0, 1, L) scans in Figure 1a,b. Different samples of identical type exhibited very similar electrochemical and structural properties in the *operando* SXRD measurements, demonstrating that the observations are highly reproducible. In some preparations mixed deposits of $\text{Co}_3\text{O}_4(111)$ and $\text{CoOOH}(001)$ were obtained, in which each of the two oxide phases exhibited its characteristic behavior, but these are not further discussed in the following. More details on the film preparation will be given in a future publication.

Additional detailed reciprocal space mapping of the Co oxide Bragg peaks, as illustrated for the cases of the $\text{Co}_3\text{O}_4(404)$ and $\text{CoOOH}(017)$ peaks (Figure 1d,e), allows refinement of

the film texture and morphology. This analysis indicates that both oxide films are composed of a thin flat film with thicker islands on top, suggesting a Stranski-Krastanov growth mode. The oxide grains exhibit a tilt distribution around the surface normal with a FWHM of $<0.5^\circ$ in both cases. For the discussed examples, the vertical / lateral coherence lengths of the oxide lattices (d_\perp / d_\parallel) derived from the Bragg peak shape analysis are 20 nm / 31 nm for the Co_3O_4 and 18 nm / 35 nm for the CoOOH film. We identify these coherence lengths with the out-of-plane and in-plane dimensions of the single crystalline grains of the oxide, respectively.

AFM studies of these samples, reveal clear differences in the surface morphology of the two oxide phases (Figure 2). The presented images were obtained after the *operando* SXRD studies presented in the following, however, very similar images were also obtained on analogously prepared as-deposited films. The CoOOH deposit (Figure 2a) appears continuous and smooth (RMS ~ 2.4 nm). Close inspection reveals well-defined terraces, separated by 0.45 ± 0.05 nm high steps. The latter is consistent with the spacing of the O-Co-OH trilayers along the c-axis (0.438 nm), which is the main structural motive of this layered compound. The typical step separation is ≈ 10 nm, but the terraces can extend by more than 100 nm in the perpendicular direction, implying that they may consist of several crystal grains of identical height. This suggests that the film consists of tightly packed grains with narrow grain boundaries, in which the lattices of the neighbouring grain nearly merge and mass transport of electrolyte species (e.g. OH ions and O_2) should be significantly impeded. In contrast, the Co_3O_4 deposit exhibits a clear granular morphology with clearly separated 3D islands (Figure 2b). The surface of islands appears rough and no steps are discernible. The average distance between neighbouring islands estimated from the AFM images is close to d_\parallel , indicating that each 3D island consists of a single oxide grain.

From these detailed structural data, the true electrochemical surface area (ECSA) of the samples can be obtained, eliminating the need to refer to other electrochemical data such as

the measured “double layer” current. Analysis of AFM images gives a roughness factor of 1.02 for CoOOH. Taking into account that the grain boundaries are apparently compact, the ECSA here must be close to the geometric surface area. For the Co₃O₄ film, the roughness determined from the AFM images is underestimated, because the tip finite size and the small island separation do not allow precise imaging of the grain boundaries. However, it may be estimated from the film morphology derived from SXRD and AFM, resulting in an ECSA that is ≈ 3 times larger than the geometric surface (supporting information, section S5). This value depends only weakly on assumptions about the islands shape and coverage (less than 20% within the spread of the experimental parameters). We consequently employ these ECSAs for the analysis of the electrochemical data.

3.2 Operando studies of the potential-dependent structure

Operando SXRD studies were conducted after injection of the 0.1 M NaOH electrolyte at a potential of 1.37 V, which is close to the measured open circuit potential. Similar characterization as in the argon atmosphere indicates that at this potential the oxide film structure remains unchanged. Subsequently, SXRD measurements during potential cycles in the range 0.77 to 1.57 V were performed, always using 1.37 V as rest potential. Two sweeps of potentials were recorded, of which only the second one is displayed for the sake of clarity, since the electrochemical current and structural data of both sweeps overlay very well.

As illustrated in Figure 3 for the Co₃O₄ sample, potential-induced changes in the film structure result in modifications in the reciprocal space position and intensity distribution of the Bragg peaks, which can be directly monitored with the 2D detector. For a quantitative determination of these changes, the peak in each detector frame was fitted in q_{\parallel} and q_{\perp} direction with pseudovoigt functions. The peak positions along q_{\parallel} and q_{\perp} directly yield the in-plane and out-of-plane strains ε_{\parallel} and ε_{\perp} in the oxide film, respectively; from the full width at

half maximum (fwhm) in these directions, the corresponding coherence lengths which are associated with the grain size d_{\parallel} and d_{\perp} are obtained. The $\text{Co}_3\text{O}_4(404)$ and $\text{CoOOH}(017)$ Bragg peaks were selected for these measurements, because they are intense and the out-of-plane structural modifications are best visible at high L-values. The high time resolution of this method (one detector image is recorded in 0.2 to 1 s), makes it possible to record these structural data during potential sweeps at rates of 10 to 50 mV/s with good potential resolution. This also allows measuring deep in the OER (up to 150 mA/cm²) without accumulating too many O₂ bubbles at the surface.

The combined electrochemical and structural data for the two types of oxides, obtained simultaneously during a potential cycle at 10 mV/s, is shown in Figure 4. The cyclic voltammogram (CV) of the $\text{Co}_3\text{O}_4(111)$ layer (red line, Figure 4a) exhibits two pairs of redox waves A1/C1 and A2/C2, superimposed on a large pseudo-capacitive current. It reproduces all features of CVs obtained with Co_3O_4 samples of various crystallinity and prepared by different methods,^{11,39,43,44} with the potentials of the redox waves approximately corresponding to the calculated equilibrium potentials for conversion of Co_3O_4 to CoOOH (A1/C1) and CoOOH to CoO_2 (A2/C2). In contrast, the CV of the $\text{CoOOH}(001)$ film (blue line) appears almost featureless with one ill-defined oxidation/reduction wave discernible around 1.2 V / 1.1 V. Table 1 gives the charge Q_0 measured in the pre-OER region (0.77 to 1.57 V) and the equivalent capacitance C_{EL} (determined in range 0.77 to 1.07 V). Note that Q_0 and C_{EL} are in the range of a few mC/cm² and mF/cm², respectively, in agreement with measurements on thin and compact cobalt oxide films.^{16,21,39}

In the *operando* SXR D studies, the structural changes in vertical and lateral grain size and strain during the CV were monitored. The results are displayed in Figs. 4b,c and Figs. 4d,e, respectively, taking the potential 0.77 V as reference state. These data evidence that the structure of the CoOOH layer (blue symbols) stays completely unaltered with $\Delta d_{\perp,\parallel} < 0.05$

nm in the entire investigated potential range and strain changes $\Delta\varepsilon_{\perp,\parallel}$ remaining below the detection limit. In contrast, the Co_3O_4 layer (red symbols) exhibits a very different behaviour, with pronounced changes during the potential cycle. Δd_{\perp} and Δd_{\parallel} pass through a shallow maximum at ≈ 1.15 V before decreasing up to the onset of OER by 1 and 4 nm, respectively (Figs. 4b,4c). The decreases in vertical grain size indicate that an ≈ 1 nm thick layer at the surface of the Co_3O_4 grains is converted into another phase, in good agreement with the results by Bergmann et al.¹¹ The larger decrease in lateral size Δd_{\parallel} indicates the formation of a slightly thicker layer (≈ 2 nm) along the sides of the grains. Scanning the potential back to 0.77 V restores $\Delta d_{\perp,\parallel} = 0$, i.e., completely reverts the skin layer back to epitaxial crystalline Co_3O_4 without any loss of material. Forward and reverse potential scan exhibit some hysteresis, with the maximum grain size in the latter being slightly lower and shifted negatively. In parallel, one observes reversible changes of both $\Delta\varepsilon_{\perp}$ and $\Delta\varepsilon_{\parallel}$ (Figure 4d,e) during the cycle. Both decrease towards positive potentials, indicating a volume change of the unit cell by ca. -1.2% between 0.77 and 1.6 V. The change is anisotropic ($\Delta\varepsilon_{\perp} > \Delta\varepsilon_{\parallel}$) which is not too surprising, since the oxide islands are in strong epitaxy with the substrate and therefore laterally clamped to its surface lattice. As $\Delta d_{\perp,\parallel}$, also $\Delta\varepsilon_{\perp,\parallel}$ exhibit small hysteresis between positive and negative going scans.

The differences between the CoOOH and the Co_3O_4 samples also are visible in simultaneous optical reflectivity measurements (Figure S8), where the former exhibits only small changes ($\approx 2\%$) whereas the latter decreases by 17% over the same potential range, which is much larger than expected for a mere surface change. In agreement with previous reports,²⁴ these reflectance changes are proportional to the pseudocapacitive charge accumulated during the potential scan (Figure S9).

In complementary measurements on this as well as other Co oxide deposits, all these structural modifications were reproducibly measured with the same amplitude upon

successive potential sweeps, even at higher sweep rates (see Figure S4). Potential step experiments further show that these modifications are fast and completed within several seconds. In addition to these potentiodynamic studies, we also measured at selected potentials the steady state structure by recording full L-rods, of the type presented in Figure 1a,b. The resulting structural data (indicated by diamonds in Figure 4b-e) agree well with those of the potentiodynamic curves. All these results demonstrate clearly that the structural changes observed for the Co_3O_4 film are a genuine potential effect, i.e., largely reflect the equilibrium structure that is characteristic for the given potential.

Extending the potential to more positive values, deep in the OER range (up to a current density of 150 mA/cm^2 , see right side panels in Figure 4b-e) does not lead to noticeable structural changes in the case of $\text{CoOOH}(001)$, indicating that this surface is extremely stable even at large current densities of oxygen evolution. For Co_3O_4 , we find a further slight decrease in $\Delta d_{\perp,\parallel}$ and $\Delta \varepsilon_{\perp,\parallel}$ with increasing OER current density. The structural parameters are very similar in the positive and the negative potential sweep, suggesting that the presence of the evolved O_2 has little influence on the oxide film structure. Plotting the thickness of the forming skin layer versus the iR -corrected voltage, reveals that the skin continues to increase approximately linearly with potential and with a similar rate $\partial d_{\perp}/\partial E \approx 2.5 \text{ nm/V}$ in OER (Figure 5a) and in the pre-OER region above 1.4 V (Figure 4b, dashed line). In the in-plane direction $\partial d_{\parallel}/\partial E \approx 12 \text{ nm/V}$ in the OER as well as in the pre-OER regime ($\geq 1.4 \text{ V}$), which corresponds to an increase by $\approx 6 \text{ nm/V}$ of the skin layer on the sides of the grains and thus is in agreement with the twofold larger thickness of this side wall skin layer found at 1.63 V. Also the strain variations take place in the entire potential range, including the OER regime.

The corresponding iR -corrected OER Tafel plots, measured in the *operando* cell in parallel to the SXRD studies and normalized to the ECSA obtained from the structural data, are shown in Figure 5b. They exhibit well-defined Tafel slopes b (given in Table 1), indicating no

major transport limitations, as expected due to the high OH^- concentration at pH 13. Obviously, both materials have rather similar current densities at moderate overpotentials, if the microscopic surface area is taken into account. Above $\approx 1 \text{ mA cm}^{-2}$ the current density of $\text{CoOOH}(001)$ becomes higher than that of the $\text{Co}_3\text{O}_4(111)$ film, reflecting its smaller Tafel slope. A more detailed analysis of the catalytic properties, focusing on the turnover frequency is provided in Table 2 of the discussion, section 4.3.

For both types of deposits, irreversible structural and morphological changes are only observed, if the cathodic potential limit becomes sufficiently negative, albeit with clear differences between the two materials. For $\text{Co}_3\text{O}_4(111)$ the grains start to significantly shrink at potentials $< 0.8 \text{ V}$ (see Figure S5), whereas for $\text{CoOOH}(001)$ such changes only occur below 0.4 V , indicating a wider stability range of the latter film. We interpret these changes as being due to the electrochemical reduction of Co_3O_4 and CoOOH into $\text{Co}(\text{OH})_2$ ^{39,43}. Upon scanning the potential back to positive values, the formed $\text{Co}(\text{OH})_2$ is not fully converted back into the epitaxial $\text{Co}_3\text{O}_4(111)$ and $\text{CoOOH}(001)$ films, respectively, resulting into an apparent loss of material. As this work focuses on the structure and properties near the OER regime, this point is not discussed in more detail here.

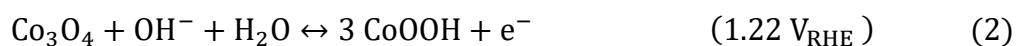
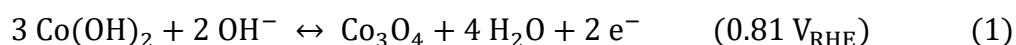
Table 1: Electrochemical data for the two oxide films. Given are the charge Q_0 derived from CVs in the pre-OER region ($0.77 - 1.57 \text{ V}$), the pseudocapacity C_{EL} , derived from the CV in the range $0.77 - 1.07 \text{ V}$, the Tafel slope b of the OER, and the current density j with respect to the ECSA at an overpotential of 400 mV .

	Q_0 (mC/cm^2)	C_{EL} (mF/cm^2)	b (mV/dec)	$j_{\text{ECSA}}(1.63 \text{ V})$ (mA cm^{-2})
$\text{Co}_3\text{O}_4(111)$	4.15	3.75	65	2.2
$\text{CoOOH}(001)$	1.4	1.2	52	3.9

4. Discussion

Our studies rely on the preparation of pure phase epitaxial $\text{Co}_3\text{O}_4(111)$ and $\text{CoOOH}(001)$ thin epitaxial layers on $\text{Au}(111)$. While the electrodeposition of epitaxial $\text{Co}_3\text{O}_4(111)$ was already demonstrated in Ref. ¹⁶, obtaining a well-defined epitaxial CoOOH layer is new.

Before starting the discussion, it is briefly recalled that, according to thermodynamics, the potential regions, where the different cobalt oxides are stable, are defined by redox reactions (1-3):^{43,45}



The discussion below is organized in different sections dealing with the stability of the $\text{CoOOH}(001)$ layer, the restructuring of the $\text{Co}_3\text{O}_4(111)$ spinel oxide near surface region and the catalytic properties of both layers. The last section discusses the pseudo capacitive current in pre-OER region.

4.1 Origin of the $\text{CoOOH}(001)$ layer stability

In view of Eqs. (1-3), the wide stability range of the $\text{CoOOH}(001)$ layer is remarkable. The CoOOH film does not exhibit structural changes down to 0.4 V (see Figure S5) and is perfectly stable in the OER region. Negative of 0.4 V, the CoOOH layer is converted most probably into $\text{Co}(\text{OH})_2$ without previous formation of the Co_3O_4 phase in an intermediate potential range. These results are in qualitative agreement with more recent thermodynamic considerations, but even here the $\text{Co}(\text{OH})_2 / \text{CoOOH}$ transition was found at more positive potentials (≤ 1.0 V vs. RHE).³² Consequently, we assign the wide stability range of the $\text{CoOOH}(001)$ film to its smooth surface, which is composed of close-packed (001)-terminated

terraces. The electrochemical reduction into $\text{Co}(\text{OH})_2$ or Co_3O_4 requires nucleation of these phases, which is expected to start at steps and point defects in the (001)-planes (see Figure 6). That this process is kinetically hindered is in accordance with the relatively small fraction of Co step edge atoms ($\approx 3\%$), estimated from the terrace width, and suggests that also the surface density of point defects is low.

In the OER range, the structural changes, characterized by $\Delta d_{\perp,\parallel}$ and $\Delta \varepsilon_{\perp,\parallel}$, are also totally absent, indicating that the CoOOH lattice remains unchanged in this range and the natural (001) cleavage plane is thus stable and is the active phase present during OER. In particular, formation of bulk crystalline CoO_2 can be excluded. Concretely, no CoO_2 formation was found in the detailed structure determination at a constant potential (Figure 4, diamonds) of 1.57 V, i.e., just above the potential where CoO_2 formation should become thermodynamically favourable, even though the potential was kept at this potential for 40 minutes. Furthermore, even short term potential excursions to ≈ 200 mV higher potentials, where the driving force for CoO_2 formation should be much higher, did not result in any structural changes. According to DFT calculations, the $\text{CoOOH}(001)$ surface termination gradually changes from OH to O in this potential regime, reaching a fully O-terminated surface at 1.5 V vs. RHE.³² Similar changes in the surface protonation state of the CoOOH grains may also occur in the grain boundaries, since these defects should allow some proton diffusion, even if the grains are tightly packed. SXRD measurements are not sensitive to such changes in the state of the surface oxygen species, because of the very small scattering cross section of hydrogen.

4.2 Potential-dependent restructuring of Co_3O_4 film surface: formation of the skin layer

The $\text{Co}_3\text{O}_4(111)$ film is stable in a much more restricted potential range than the smooth $\text{CoOOH}(001)$ layer. At potentials more negative than 0.8 V (Figure S5), transformation into the more thermodynamically stable phase $\text{Co}(\text{OH})_2$ commences and above this potential,

small reversible structural changes take place at the surface and also in the bulk. In this section, we specifically focus on surface modifications in the potential range 0.77 – 1.7 V, i.e., the variations of $\Delta d_{\perp,\parallel}$. The volume modifications ($\Delta \varepsilon_{\perp,\parallel}$) will be discussed in the final section of this paper.

The good agreement between the values of $d_{\perp,\parallel}$ and the dimension of the 3D islands imaged by AFM indicates that the latter consist of single grains and are directly probed by the *operando* SXRD measurements. The small changes in $\Delta d_{\perp,\parallel}$ between 0.77 and 1.0 V can be assigned to a gradual onset of the $\text{Co(OH)}_2/\text{Co}_3\text{O}_4$ transition in the first atomic planes. Between 1.2 V and 1.67 V, the changes in $\Delta d_{\perp,\parallel}$ indicate the fully reversible formation of a ≈ 1 nm thick skin layer on the top and side walls of the grains.

This observation is in excellent agreement with the previous results by Bergmann et al. for polycrystalline Co_3O_4 .¹¹ However, the time and potential resolved data obtained in our study provide important additional insights into the formation mechanism and nature of this skin layer.

Our first main observation is that the skin layer emerges ≈ 300 mV negative of the onset of OER and thus is not directly related to the catalytic reaction as previously assumed. In these earlier studies, identification of the skin layer with an amorphous or highly defective $\text{CoO}_x(\text{OH})_y$ phase was proposed on the basis of X-ray spectroscopy and photoemission data.^{11,20,21} Furthermore, the skin layer was only observed at one potential (1.62 V) in the OER regime and thus thought to be caused by this reaction. The results presented here indicate that this near surface restructuring rather reflects the thermodynamics of the $\text{Co}_3\text{O}_4/\text{CoOOH}$ phase transition, because its formation starts at a potential close to the equilibrium potential of reaction (2). In explaining this structural transition, we have to consider that it is not only fast but also fully reversible, which excludes simple kinetic effects, such as slow skin layer growth. We have also to take into account that the skin layer is not

accompanied by cobalt dissolution into the electrolyte, as evidenced by the absence of any irreversible loss of Co_3O_4 for potentials ≥ 1 V. This is seen in the *operando* studies during CVs (as e.g. in Figure 4) as well as in auxiliary experiments where the sample was found to be completely stable for many hours at 1.4 V, i.e., a potential in the range of the skin layer.

In an atomistic picture, the formation of a skin layer in pre-OER region plausibly relies on displacements of the Co^{2+} cations from tetrahedral to octahedral symmetry because the Co oxidation state increases from $\text{Co}^{2+}/\text{Co}^{3+}$ to Co^{3+} for potentials above 1.2 V. This restructuring requires significant transport of oxygen and Co ions through the oxide lattice. However, because the skin layer is only of nm-thickness, this transport still can be rapid, which explains why the skin layer forms rapidly and is reversibly converted back into epitaxial Co_3O_4 upon reverting the potential to more negative values. In the OER region, the cobalt redox state increases further from Co^{3+} to $\text{Co}^{3+}/\text{Co}^{4+}$ ^{11,20,21} but this does not imply further modification of the Co local O-coordination shell, explaining why the skin thickness is only weakly affected by the catalytic reaction. It is noted in this context that even in our epitaxial systems the skin layer does not form on a perfectly smooth $\text{Co}_3\text{O}_4(111)$ surface, but on nanoscale 3D islands that expose other facets to the electrolyte (most probably $\text{Co}_3\text{O}_4(100)$).^{46,47} This might facilitate the layer formation, e.g. by providing channels for cation (vacancy) migration within the oxygen framework. Indeed, the ≈ 4 times larger potential-dependence in the in-plane as compared to the out of plane direction may be rationalized by more facile ion migration parallel to the (111)-planes (see below).

Our second main observation regarding the skin layer is that its thickness is a linear function of applied potential. Namely, it gradually increases with identical slopes $\partial d_{\perp,\parallel}/\partial E$ in the pre-OER and in the OER range, confirming that the oxygen evolution reaction does not substantially affect the skin layer growth. In other words, the thickness is determined by applied electrode potential alone. The linear change of the skin layer thickness with potential

strongly resembles the behaviour of passive films and implies the presence of a constant electric field within the skin layer, which is independent of the potential. Thus, also for the oxide system studied here, models developed for describing passive film formation on iron group metals may be applicable, in particular since for those passive films often a duplex structure was reported, consisting of two stacked layers of different oxide phases.^{48,49} These models should be well suited to describe skin layer formation on oxides, as found in the Co_3O_4 system, since they likewise describe the formation of a kinetically limited surface layer, consisting of cation species in a higher oxidation state and (additional) oxygen anions, due to a thermodynamic driving force. Whether this is an oxide layer on a metal or a (hydr)oxide layer on an oxide substrate should *per se* not matter fundamentally. Unfortunately, many models of passive film growth yield a linear variation of the layer thickness, for example, the high field model, the point defect model, and variations of those (see Refs. ^{50,51} and references therein). Unambiguous identification of the skin layer formation mechanism thus will require much more detailed data, e.g., on its dependence on pH and the growth kinetics, that will allow to distinguish between the different scenarios.

4.3 Catalytic properties and structure of active sites

On the basis of the structural results, we will now discuss the catalytic properties of our epitaxial samples. The *b*-value of $\text{Co}_3\text{O}_4(111)$ and $\text{CoOOH}(001)$ films given in Table 1 are in good agreement with that reported by Switzer and co-workers for μm thick electrodeposited epitaxial Co_3O_4 layers¹⁶ and exfoliated CoOOH nanosheets.^{37,38} Table 2 gives the turnover frequency of our samples and the overpotential that is necessary to flow a current density of 10 mAcm^{-2} . The latter parameter compares very well with literature, even for the smooth $\text{CoOOH}(001)$ films, if one accounts for the true microscopic surface area. The reported TOF

is defined here as the number of O₂ molecules generated per second and per surface site. As surface site, we consider any Co-O surface bond. Details for the calculation of the TOF are given in the supplementary information (section S5). For CoOOH(001) layers we find a TOF of $\approx 4.2 \text{ s}^{-1}$ which is in between that of thick CoOOH(001) oriented films of known ECSA¹³ and that of exfoliated CoOOH nanosheets.^{37,38} We consider these examples because the surface structure of these samples is *a priori* the closest to that of our sample. In the case of the Co₃O₄(111) layer, it is not possible to calculate a TOF with the above definition, since the real density of sites in the 3D skin layer is unknown. Assuming conservatively only sites on the surface are active, we estimate a TOF $\approx 3.2 \text{ s}^{-1}$, as explained in section S5, for the purpose of comparison with CoOOH and literature. We have to bear in mind that this value of $\approx 3.2 \text{ s}^{-1}$ only represents the order of magnitude of the TOF. It is yet much larger than most of those reported in the literature for Co₃O₄ and CoCat (see Table 2) and compares well with only a few references. This point will be addressed in more detail later on.

Table 2: Estimated TOF for $\eta = 0.4$ V and overpotential η for a current density of $j = 10$ mA/cm² with respect to the ECSA. TOF values reported in the literature are given for comparison.

Oxide	Structure/morphology	TOF (s ⁻¹) ($\eta = 0.4$ V)	η (V) ($j = 10$ mA/cm ²)	Ref.
CoOOH(001)	Epitaxial (001)	4.2	0.42	This work 13
	Oriented (001)	0.4 ^{a)}	0.43	38
	Exfoliated nanosheets	15 ^{b)}	0.3	37
	Exfoliated nanosheets	0.023 ^{b)}	0.39	
Co ₃ O ₄ (111)	Epitaxial (111)/Au	3.2	0.42	This work 13
	Epitaxial (111)/Au	0.4 ^{a)}	0.43	
Poly-Co ₃ O ₄	Nanocrystalline	1.36 10 ^{-3 c)}	0.44	11
	Nanocrystalline/Au (80ML)	5 · 10 ^{-2 c)}	na	52
	Nanocrystalline/Au (0.4ML)	1.5 ^{c)}	na	52
CoCat	amorphous	8 10 ^{-4 b)}		53

a) Estimated using ECSA derived from capacitance measurements in acetonitrile

b) Estimated assuming all Co centres within the material are active

c) Estimated using ECSA derived from capacitance measurements in aqueous alkaline electrolyte

At this stage, our main finding is that a smooth epitaxial CoOOH(001) layer with a well-defined structure is nearly as good catalyst as a Co₃O₄(111) layer or any Co₃O₄ catalyst of the literature, if one accounts for the true microscopic surface area. This is in contrast with general assumptions in literature and not easy to reconcile with the current conceptions on the nature of the OER-active site on Co oxide catalysts. Moreover, reaching these catalytic performances does not require “pre-conditioning” of the CoOOH film, because it is structurally stable. This last point appears again to be in contrast with the general behavior reported in the literature (see for instance ^{19,37}) and reinforces the interest of studying well-defined epitaxial films.

It was proposed in previous studies of amorphous CoCat catalyst films³⁰ that the OER active sites are di- μ -oxo-bridged (μ_2 -O) ion clusters, in which Co atoms are in a near-octahedral coordination by 6 oxygen ligands with a Co-Co distance is 2.81 Å and oxygen

atoms bound to two Co atoms only, a configuration which is similar to that in Co-oxo cubanes.⁵⁴ On the (001) plane of CoOOH, only μ_3 -O/OH sites exist, where the oxygen is threefold coordinated to Co^{3+} , and μ_2 -O configurations only exist at steps of CoOOH(100) surface or near Co^{3+} surface vacancies (Figure 6). According to our structural data, the coverage of μ_2 -O/OH sites on our CoOOH is only a few percent. Assuming that the latter are the predominant active sites of the OER, the reaction would occur at a small fraction of the surface sites only and the true TOF would be of the order of 100 s^{-1} .

In the case of the $\text{Co}_3\text{O}_4(111)$ film, we have seen previously that a skin layer is covering the islands (see scheme in Figure 4, top right corner) before the OER, which is only marginally thickening further in OER. This skin layer is probably a highly defective, 3D reaction zone for the OER, in analogy with the behaviour of CoCat.³⁴ It should therefore be more active than a smooth CoOOH(001) film since defects are thought to improve the catalytic activity.⁵⁵ In previous studies, it was concluded on the basis of XAS measurements that the skin layer consists of a $\text{Co}_x(\text{OH})_y$ phase with an increased amount of octahedrally coordinated di- μ -O/OH-bridged $\text{Co}^{3+/4+}$ ions and these sites were considered as indispensable for the OER activity of Co_3O_4 .¹¹ The very similar activity of Co_3O_4 and CoOOH in our study is therefore difficult to rationalize in this scenario and can only be explained in two different ways: Either, the number of μ_2 -O/OH sites in the skin layer is only a few percent of the ECSA, which seems unlikely because a strong local structural disorder is expected within the skin, or the high catalytic activity of the CoOOH(001) surface is not caused by μ_2 -O/OH sites alone and other sites of this surface, specifically μ_3 -O/OH sites, significantly contribute to the OER. The latter seems not unlikely, taking into account that in μ_2 -O/OH and μ_3 -O/OH sites the Co-O bond length and the spacing of the oxygen atom to neighbouring O is very similar. At least in terms of the local geometry, the OER reaction mechanisms proposed in previous studies^{11,28} therefore should be possible for both sites.

4.4 Pseudo capacitive charge in per OER region

We now discuss the electrochemical charge Q_0 measured in the pre-OER region (Table 1). As explained in section S6, for CoOOH(001) the charge $Q_0 \approx 1.4 \text{ mC cm}^{-2}$ may be attributed simply to adsorption/desorption on the oxide surface, specifically protonation / deprotonation of the outermost oxygen atoms on the top surface plane and within the grain boundaries. According to a previous DFT study, the deprotonation of the CoOOH(001) surface indeed extends over a wide potential regime, with the stability ranges of the fully H-terminated and the fully O-terminated surface at $\leq 0.3 \text{ V}$ and $\geq 1.5 \text{ V}$ vs. RHE, respectively.³² We note, as an additional proof that the changes in the optical reflectivity of this sample are consistent with a surface effect (supporting information, section S7, Fig. S8). A pure surface charging is further in agreement with the absence of structural modifications in the pre-OER region.

In the case of Co_3O_4 , the charge $Q_0 \approx 4.15 \text{ mC/cm}^2$ for the sample in Figure 4 corresponds to a charge $q_0 = 0.86 e_0$ per formula unit of oxide within the deposited film (see supporting information, section S6) which reduces to $q_0 = 0.58 e_0$ after subtraction of the charge necessary to form the 1 nm thick skin. A logical conclusion is that the pseudo-capacitive charge transfer involves the bulk of the Co_3O_4 epitaxial film. This is also supported by the optical reflectivity measurements, which mirror the corresponding charge transfer (see section S7, Figure S9a) and is in accordance with previous observations for CoCat.²⁴ The changes in the bulk charge state are probably linked to the reversible changes in unit cell volume, which occur in the same potential region. This is also in agreement with XAS results that likewise found a decrease in bond distances upon oxidation of Co^{2+} to Co^{3+} .¹¹ Furthermore, these fast and reversible bulk structural changes explain the excellent performances and cyclability of Co_3O_4 in supercapacitor applications.⁵⁶

A pending question is the identification of the charges associated with the substantial pseudo-capacitive charge / discharge in Co_3O_4 . The discussion must also take into account the rate of this process, which is fast (≤ 1 s for anodic charging) for a bulk phenomenon. If this process would be related to a bulk Co redox reaction, the predominant fraction of the Co^{2+} ions in the 20 nm thick Co_3O_4 film would have to be converted into Co^{3+} . This seems very unlikely, given that the spinel lattice is largely maintained and that the mean oxidation state of the material remains close to that of the spinel phase. In previous studies, intercalation of solution species, such as cations or hydroxyls, was proposed to explain the large pseudo-capacitive current,^{13,57} which is sustained by the fact that no such bulk charging is observed in organic electrolyte, such as acetonitrile (interfacial capacitance is of the order of a few $10\mu\text{F}/\text{cm}^2$ in this solvent).^{13,16} More work is necessary to check this hypothesis and identify the nature of the bulk charge transfer.

An important practical consequence of these findings is that, contrary to general practice in electrocatalytic studies of Co oxide materials, the current in the pre-OER range cannot be easily employed to estimate the electrochemical surface area or redox-active surface sites. Concretely, dividing the pseudo-capacitance of the oxide by a standard double layer capacitance of $60\mu\text{F}/\text{cm}^2$, as usually done in literature,^{5,12} leads to an erroneous electrochemical surface area (ECSA) that is several orders of magnitude larger than derived from independent structural characterization. This has already been noted in previous studies^{16,27,58} where the ECSA was estimated by other methods (e.g. impedance measurements in an organic solvent), but has been largely ignored in the community. Our results for structurally well-characterized samples reinforce the need for independent ECSA determination as good practice in electrocatalytic studies of Co oxides.

5. Conclusions

In summary, we studied the OER on Co oxides by combining structurally well-defined model catalysts – thin epitaxial $\text{Co}_3\text{O}_4(111)$ and $\text{CoOOH}(001)$ films – and advanced *operando* X-ray surface diffraction techniques. This approach enables direct correlation of the potential-dependent microscopic surface structure and the electrochemical current, which are measured simultaneously. It specifically allows independent determination of the electrochemical surface area and thus straightforward comparison of the catalytic activity.

According to our results, $\text{Co}_3\text{O}_4(111)$ and $\text{CoOOH}(001)$ behave quite differently from a structural viewpoint, whereas their catalytic performances appear very similar, suggesting that the two materials have a similar surface density of OER active sites. The surface structure of $\text{CoOOH}(001)$ is very stable, even at high OER current densities. It is primarily terminated by oxygen atoms that are threefold Co-coordinated ($\mu_3\text{-O}$) and only exhibits a small number of the di- μ -oxo bridged Co sites ($\mu_2\text{-O}$) at surface defects (steps and terrace cation vacancies), that are typically associated with the good OER activity of cobalt oxides.

On $\text{Co}_3\text{O}_4(111)$, the OER occurs on a skin layer, whose formation is highly reversible, fast, and commences in the pre-OER range, near the $\text{CoOOH} / \text{Co}_3\text{O}_4$ equilibrium potential, indicating that it is not induced by the catalytic reaction, but reflects the oxide electrochemistry. The skin layer thickness is increasing almost linearly with potential, even in the OER regime. We suggest that this behaviour may be explained by models derived for passive film formation. Following the current assumption in the literature that the skin layer corresponds to a defective 3D reaction zone with a high number of $\mu_2\text{-O}$ sites, the very similar catalytic properties of Co_3O_4 and $\text{CoOOH}(001)$ suggests that the $\mu_3\text{-O}$ sites may also contribute to the OER on the latter surface.

In addition, we find over a wide potential range reversible changes of the bulk lattice constant (i.e. a change in the density of the Co_3O_4 film) which may be attributed to the

reversible creation / annihilation of a high density of volume stoichiometric defects. Together with the charge caused by skin layer formation/removal, these seem to be associated with the large pseudo-capacitive current of this material in the pre-OER range, a phenomenon that also explains why this oxide is a good material for supercapacitor applications.

Supporting Information

Details of the data analysis and additional figures and results are available free of charge via the Internet at <http://pubs.acs.org/>.

Acknowledgements

We gratefully acknowledge financial support by the Agence Nationale de la Recherche (ANR) and the Deutsche Forschungsgemeinschaft (DFG) via project EC-MEC (ANR-15-CE30-0024-01 and Ma1618/2020) and thank the ESRF / ID03 beamline staff, in particular Francesco Carla, for technical support.

References

- (1) Lewis, N. S., Nocera, D. G., Powering the Planet: Chemical Challenges in Solar Energy Utilization, *Proceedings of the National Academy of Sciences*, **2006**, *103*, 15729.
- (2) Kanan, M. W., Nocera, D. G., In Situ Formation of an Oxygen-Evolving Catalyst in Neutral Water Containing Phosphate and Co^{2+} , *Science*, **2008**, *321*, 1072-1075.
- (3) Deng, X., Tüysüz, H., Cobalt-Oxide-Based Materials as Water Oxidation Catalyst: Recent Progress and Challenges, *ACS Catalysis*, **2014**, *4*, 3701-3714.
- (4) Suen, N.-T., Hung, S.-F., Quan, Q., Zhang, N., Xu, Y.-J., Chen, H. M., Electrocatalysis for the Oxygen Evolution Reaction: Recent Development and Future Perspectives, *Chemical Society Reviews*, **2017**, *46*, 337-365.
- (5) McCrory, C. C. L., Jung, S., Ferrer, I. M., Chatman, S. M., Peters, J. C., Jaramillo, T. F., Benchmarking Hydrogen Evolving Reaction and Oxygen Evolving Reaction Electrocatalysts for Solar Water Splitting Devices, *Journal of the American Chemical Society*, **2015**, *137*, 4347-4357.
- (6) Burke, M. S., Zou, S., Enman, L. J., Kellon, J. E., Gabor, C. A., Pledger, E., Boettcher, S. W., Revised Oxygen Evolution Reaction Activity Trends for First-Row Transition-Metal (Oxy)Hydroxides in Alkaline Media, *The Journal of Physical Chemistry Letters*, **2015**, *6*, 3737-3742.
- (7) Doyle, R. L., Godwin, I. J., Brandon, M. P., Lyons, M. E. G., Redox and Electrochemical Water Splitting Catalytic Properties of Hydrated Metal Oxide Modified Electrodes, *Phys. Chem. Chem. Phys.*, **2013**, *15*, 13737-13783.
- (8) Pirovano, C., Trasatti, S., The Point of Zero Charge of Co_3O_4 : Effect of the Preparation Procedure, *Journal of Electroanalytical Chemistry and Interfacial Electrochemistry*, **1984**, *180*, 171-184.
- (9) Yuming, D., Kun, H., Lin, Y., Aimin, Z., A Facile Route to Controlled Synthesis of Co_3O_4 Nanoparticles and Their Environmental Catalytic Properties, *Nanotechnology*, **2007**, *18*, 435602-435602.
- (10) Alvarado, S. R., Guo, Y., Ruberu, T. P. A., Bakac, A., Vela, J., Photochemical Versus Thermal Synthesis of Cobalt Oxyhydroxide Nanocrystals, *The Journal of Physical Chemistry C*, **2012**, *116*, 10382-10389.
- (11) Bergmann, A., Martinez-Moreno, E., Teschner, D., Chernev, P., Gliech, M., de Araújo, J. F., Reier, T., Dau, H., Strasser, P., Reversible Amorphization and the Catalytically Active State of Crystalline Co_3O_4 During Oxygen Evolution, *Nature Communications*, **2015**, *6*, 8625.
- (12) Esswein, A. J., McMurdo, M. J., Ross, P. N., Bell, A. T., Tilley, T. D., Size-Dependent Activity of Co_3O_4 Nanoparticle Anodes for Alkaline Water Electrolysis, *The Journal of Physical Chemistry C*, **2009**, *113*, 15068-15072.
- (13) Hull, C. M., Koza, J. A., Switzer, J. A., Electrodeposition of Epitaxial $\text{Co}(\text{OH})_2$ on Gold and Conversion to Epitaxial CoOOH and Co_3O_4 , *J. Mater. Res.*, **2016**, *31*, 3324-3331.
- (14) Friebel, D., Bajdich, M., Yeo, B. S., Louie, M. W., Miller, D. J., Sanchez Casalongue, H., Mbuga, F., Weng, T.-C., Nordlund, D., Sokaras, D., Alonso-Mori, R., Bell, A. T., Nilsson, A., On the Chemical State of Co Oxide Electrocatalysts During Alkaline Water Splitting, *Phys. Chem. Chem. Phys.*, **2013**, *15*, 17460-17467.
- (15) Surendranath, Y., Dincă, M., Nocera, D. G., Electrolyte-Dependent Electrosynthesis and Activity of Cobalt-Based Water Oxidation Catalysts, *Journal of the American Chemical Society*, **2009**, *131*, 2615-2620.
- (16) Koza, J. A., He, Z., Miller, A. S., Switzer, J. A., Electrodeposition of Crystalline Co_3O_4 —a Catalyst for the Oxygen Evolution Reaction, *Chem. Mat.*, **2012**, *24*, 3567-3573.
- (17) Stevens, M. B., Enman, L. J., Batchelor, A. S., Cosby, M. R., Vise, A. E., Trang, C. D. M., Boettcher, S. W., Measurement Techniques for the Study of Thin Film Heterogeneous Water Oxidation Electrocatalysts, *Chem. Mat.*, **2017**, *29*, 120-140.
- (18) Song, F., Bai, L., Moysiadou, A., Lee, S., Hu, C., Liardet, L., Hu, X., Transition Metal Oxides as Electrocatalysts for the Oxygen Evolution Reaction in Alkaline Solutions: An Application-Inspired Renaissance, *Journal of the American Chemical Society*, **2018**, *140*, 7748-7759.
- (19) Bergmann, A., Jones, T. E., Martinez Moreno, E., Teschner, D., Chernev, P., Gliech, M., Reier, T., Dau, H., Strasser, P., Unified Structural Motifs of the Catalytically Active State of

- Co(Oxyhydr)Oxides During the Electrochemical Oxygen Evolution Reaction, *Nature Catalysis*, **2018**, *1*, 711-719.
- (20) Tung, C.-W., Hsu, Y.-Y., Shen, Y.-P., Zheng, Y., Chan, T.-S., Sheu, H.-S., Cheng, Y.-C., Chen, H. M., Reversible Adapting Layer Produces Robust Single-Crystal Electrocatalyst for Oxygen Evolution, *Nature Communications*, **2015**, *6*, 8106.
- (21) Favaro, M., Yang, J., Nappini, S., Magnano, E., Toma, F. M., Crumlin, E. J., Yano, J., Sharp, I. D., Understanding the Oxygen Evolution Reaction Mechanism on CoOx Using Operando Ambient-Pressure X-Ray Photoelectron Spectroscopy, *Journal of the American Chemical Society*, **2017**, *139*, 8960-8970.
- (22) Giordano, L., Han, B., Risch, M., Hong, W. T., Rao, R. R., Stoerzinger, K. A., Shao-Horn, Y., Ph Dependence of Oer Activity of Oxides: Current and Future Perspectives, *Catalysis Today*, **2016**, *262*, 2-10.
- (23) van Oversteeg, C. H. M., Doan, H. Q., de Groot, F. M. F., Cuk, T., In Situ X-Ray Absorption Spectroscopy of Transition Metal Based Water Oxidation Catalysts, *Chemical Society Reviews*, **2017**, *46*, 102-125.
- (24) Risch, M., Ringleb, F., Kohlhoff, M., Bogdanoff, P., Chernev, P., Zaharieva, I., Dau, H., Water Oxidation by Amorphous Cobalt-Based Oxides: In Situ Tracking of Redox Transitions and Mode of Catalysis, *Energy & Environmental Science*, **2015**, *8*, 661-674.
- (25) Yang, J., Cooper, J. K., Toma, F. M., Walczak, K. A., Favaro, M., Beeman, J. W., Hess, L. H., Wang, C., Zhu, C., Gul, S., Yano, J., Kisielowski, C., Schwartzberg, A., Sharp, I. D., A Multifunctional Biphasic Water Splitting Catalyst Tailored for Integration with High-Performance Semiconductor Photoanodes, *Nat Mater*, **2017**, *16*, 335-341.
- (26) Ullman, A. M., Brodsky, C. N., Li, N., Zheng, S.-L., Nocera, D. G., Probing Edge Site Reactivity of Oxidic Cobalt Water Oxidation Catalysts, *Journal of the American Chemical Society*, **2016**, *138*, 4229-4236.
- (27) Amin, H. M. A., Baltruschat, H., How Many Surface Atoms in Co₃O₄ Take Part in Oxygen Evolution? Isotope Labeling Together with Differential Electrochemical Mass Spectrometry, *Phys. Chem. Chem. Phys.*, **2017**, *19*, 25527-25536.
- (28) Zhang, M., de Respinis, M., Frei, H., Time-Resolved Observations of Water Oxidation Intermediates on a Cobalt Oxide Nanoparticle Catalyst, *Nat Chem*, **2014**, *6*, 362-367.
- (29) Zhang, M., Frei, H., Water Oxidation Mechanisms of Metal Oxide Catalysts by Vibrational Spectroscopy of Transient Intermediates, *Annual Review of Physical Chemistry*, **2017**, *68*, 209-231.
- (30) Risch, M., Khare, V., Zaharieva, I., Gerencser, L., Chernev, P., Dau, H., Cobalt-Oxo Core of a Water-Oxidizing Catalyst Film, *Journal of the American Chemical Society*, **2009**, *131*, 6936-6937.
- (31) Bajdich, M., García-Mota, M., Vojvodic, A., Nørskov, J. K., Bell, A. T., Theoretical Investigation of the Activity of Cobalt Oxides for the Electrochemical Oxidation of Water, *Journal of the American Chemical Society*, **2013**, *135*, 13521-13530.
- (32) Chen, J., Selloni, A., First Principles Study of Cobalt (Hydr)Oxides under Electrochemical Conditions, *The Journal of Physical Chemistry C*, **2013**, *117*, 20002-20006.
- (33) Plaisance, C. P., van Santen, R. A., Structure Sensitivity of the Oxygen Evolution Reaction Catalyzed by Cobalt(Ii,Iii) Oxide, *Journal of the American Chemical Society*, **2015**, *137*, 14660-14672.
- (34) Klingan, K., Ringleb, F., Zaharieva, I., Heidkamp, J., Chernev, P., Gonzalez-Flores, D., Risch, M., Fischer, A., Dau, H., Water Oxidation by Amorphous Cobalt-Based Oxides: Volume Activity and Proton Transfer to Electrolyte Bases, *ChemSusChem*, **2014**, *7*, 1301-1310.
- (35) Zhang, M., Frei, H., Towards a Molecular Level Understanding of the Multi-Electron Catalysis of Water Oxidation on Metal Oxide Surfaces, *Catalysis Letters*, **2015**, *145*, 420-435.
- (36) Xiao, J., Kuang, Q., Yang, S., Xiao, F., Wang, S., Guo, L., Surface Structure Dependent Electrocatalytic Activity of Co₃O₄ Anchored on Graphene Sheets toward Oxygen Reduction Reaction, *Scientific Reports*, **2013**, *3*, 2300.
- (37) Song, F., Hu, X., Exfoliation of Layered Double Hydroxides for Enhanced Oxygen Evolution Catalysis, *Nature Communications*, **2014**, *5*, 4477.

- (38) Huang, J., Chen, J., Yao, T., He, J., Jiang, S., Sun, Z., Liu, Q., Cheng, W., Hu, F., Jiang, Y., Pan, Z., Wei, S., Cooh Nanosheets with High Mass Activity for Water Oxidation, *Angewandte Chemie International Edition*, **2015**, *54*, 8722-8727.
- (39) Faisal, F., Bertram, M., Stumm, C., Cherevko, S., Geiger, S., Kasian, O., Lykhach, Y., Lytken, O., Mayrhofer, K. J. J., Brummel, O., Libuda, J., Atomically Defined $\text{Co}_3\text{O}_4(111)$ Thin Films Prepared in Ultrahigh Vacuum: Stability under Electrochemical Conditions, *The Journal of Physical Chemistry C*, **2018**, *122*, 7236-7248.
- (40) Wang, J., Ocko, B. M., Davenport, A. J., Isaacs, H. S., In Situ X-Ray-Diffraction and -Reflectivity Studies of the $\text{Au}(111)$ /Electrolyte Interface: Reconstruction and Anion Adsorption, *Phys. Rev. B*, **1992**, *46*, 10321-10338.
- (41) Liu, X., Prewitt, C. T., High-Temperature X-Ray Diffraction Study of Co_3O_4 : Transition from Normal to Disordered Spinel, *Physics and Chemistry of Minerals*, **1990**, *17*, 168-172.
- (42) Delaplane, R. G., Ibers, J. A., Ferraro, J. R., Rush, J. J., Diffraction and Spectroscopic Studies of the Cobaltic Acid System $\text{HCoC}_2\text{-DCoO}_2$, *The Journal of Chemical Physics*, **1969**, *50*, 1920-1927.
- (43) Behl, W. K., Toni, J. E., Anodic Oxidation of Cobalt in Potassium Hydroxide Electrolytes, *Journal of Electroanalytical Chemistry and Interfacial Electrochemistry*, **1971**, *31*, 63-75.
- (44) Trasatti, S., Petrii, O. A., Real Surface Area Measurements in Electrochemistry, *J. Electroanal. Chem.*, **1992**, *327*, 353-376.
- (45) Binninger, T., Mohamed, R., Waltar, K., Fabbri, E., Levecque, P., Kötz, R., Schmidt, T. J., Thermodynamic Explanation of the Universal Correlation between Oxygen Evolution Activity and Corrosion of Oxide Catalysts, *Scientific Reports*, **2015**, *5*, 12167.
- (46) García-Mota, M., Bajdich, M., Viswanathan, V., Vojvodic, A., Bell, A. T., Nørskov, J. K., Importance of Correlation in Determining Electrocatalytic Oxygen Evolution Activity on Cobalt Oxides, *The Journal of Physical Chemistry C*, **2012**, *116*, 21077-21082.
- (47) Zasada, F., Gryboś, J., Piskorz, W., Sojka, Z., Cobalt Spinel (111) Facets of Various Stoichiometry—Dft+U and Ab Initio Thermodynamic Investigations, *The Journal of Physical Chemistry C*, **2018**, *122*, 2866-2879.
- (48) Vetter, K. J., General Kinetics of Passive Layers on Metals, *Electrochim. Acta*, **1971**, *16*, 1923-1937.
- (49) Badawy, W. A., Al-Kharafi, F. M., Al-Ajmi, J. R., Electrochemical Behaviour of Cobalt in Aqueous Solutions of Different Ph, *J. Appl. Electrochem.*, **2000**, *30*, 693-704.
- (50) Macdonald, D. D., The History of the Point Defect Model for the Passive State: A Brief Review of Film Growth Aspects, *Electrochim. Acta*, **2011**, *56*, 1761-1772.
- (51) Veluchamy, A., Sherwood, D., Emmanuel, B., Cole, I. S., Critical Review on the Passive Film Formation and Breakdown on Iron Electrode and the Models for the Mechanisms Underlying Passivity, *J. Electroanal. Chem.*, **2017**, *785*, 196-215.
- (52) Yeo, B. S., Bell, A. T., Enhanced Activity of Gold-Supported Cobalt Oxide for the Electrochemical Evolution of Oxygen, *Journal of the American Chemical Society*, **2011**, *133*, 5587-5593.
- (53) Surendranath, Y., Kanan, M. W., Nocera, D. G., Mechanistic Studies of the Oxygen Evolution Reaction by a Cobalt-Phosphate Catalyst at Neutral Ph, *Journal of the American Chemical Society*, **2010**, *132*, 16501-16509.
- (54) Ama, T., Rashid, M. M., Yonemura, T., Kawaguchi, H., Yasui, T., Cobalt(III) Complexes Containing Incomplete Co_3O_4 or Complete Co_4O_4 Cubane Core, *Coordination Chemistry Reviews*, **2000**, *198*, 101-116.
- (55) Zhang, R., Zhang, Y.-C., Pan, L., Shen, G.-Q., Mahmood, N., Ma, Y.-H., Shi, Y., Jia, W., Wang, L., Zhang, X., Xu, W., Zou, J.-J., Engineering Cobalt Defects in Cobalt Oxide for Highly Efficient Electrocatalytic Oxygen Evolution, *ACS Catalysis*, **2018**, *8*, 3803-3811.
- (56) Deng, T., Zhang, W., Arcelus, O., Kim, J.-G., Carrasco, J., Yoo, S. J., Zheng, W., Wang, J., Tian, H., Zhang, H., Cui, X., Rojo, T., Atomic-Level Energy Storage Mechanism of Cobalt Hydroxide Electrode for Pseudocapacitors, *Nature Communications*, **2017**, *8*, 15194.
- (57) Boggio, R., Carugati, A., Trasatti, S., Electrochemical Surface Properties of Co_3O_4 Electrodes, *J. Appl. Electrochem.*, **1987**, *17*, 828-840.

(58) Liu, Y.-C., Koza, J. A., Switzer, J. A., Conversion of Electrodeposited Co(OH)_2 to CoOOH and Co_3O_4 , and Comparison of Their Catalytic Activity for the Oxygen Evolution Reaction, *Electrochim. Acta*, **2014**, *140*, 359-365.

Figures:

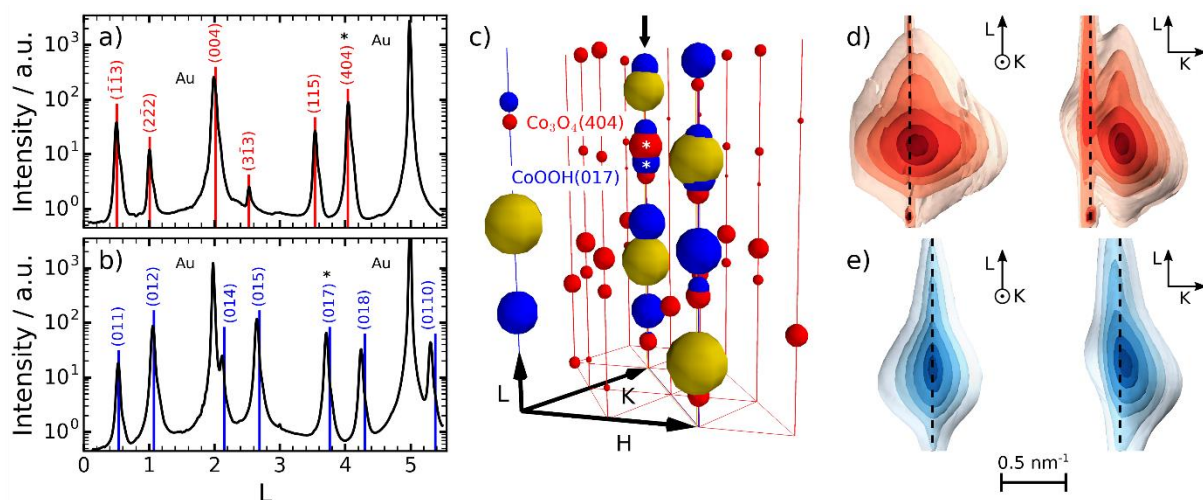


Figure 1: Scans along the (0, 1, L) crystal truncation rods of oxide films electrodeposited in (a) 2 M and (b) 5 M NaOH, demonstrating the epitaxial growth of (a) pure $\text{Co}_3\text{O}_4(111)$ and (b) pure $\text{CoOOH}(001)$. The expected positions of the Bragg peaks for (unstrained) bulk Co_3O_4 and CoOOH are indicated by red and blue lines, respectively. (c) Corresponding schematic reciprocal space geometry, showing the Bragg peaks and crystal truncation rods of the $\text{Au}(111)$ substrate (yellow), $\text{Co}_3\text{O}_4(111)$ (red) and $\text{CoOOH}(001)$ (blue). The axes H, K and L indicate the hexagonal unit cell of the $\text{Au}(111)$ substrate. (d,e) Reciprocal space maps of (d) the $\text{Co}_3\text{O}_4(404)$ and (e) the $\text{CoOOH}(017)$ Bragg peaks (marked by * in a-c).

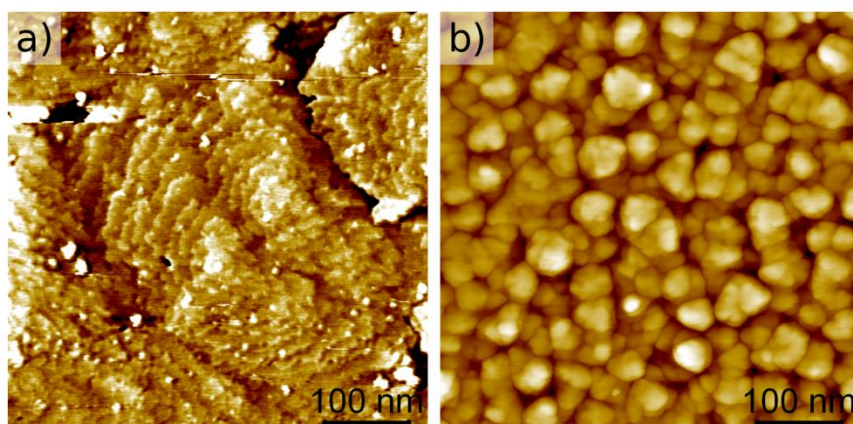


Figure 2: AFM images (500 nm x 500 nm) of (a) CoOOH(001) and (b) Co₃O₄(111) layers electrodeposited on Au(111). Films are 18 and 20 nm thick, respectively, and were recorded after the *operando* SXRD studies on the samples shown in Figure 1a,b.

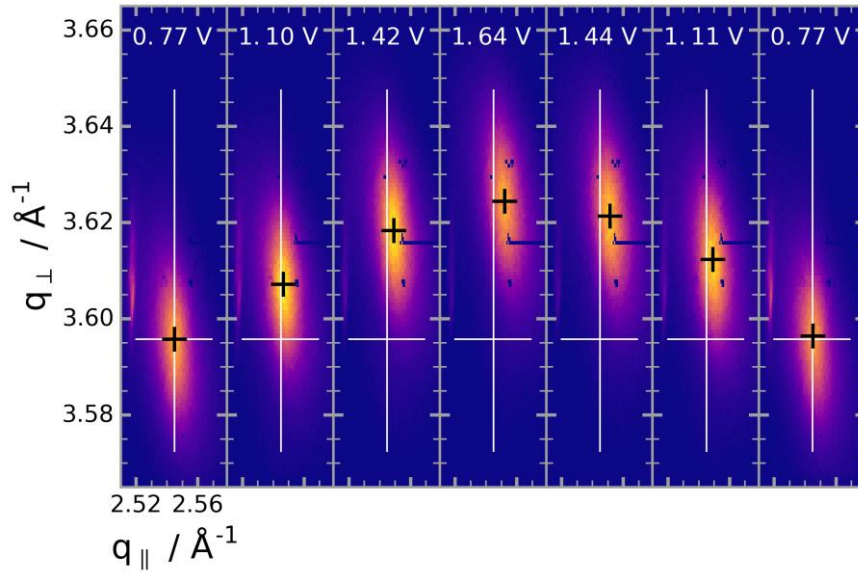


Figure 3: X-ray detector images, illustrating the reversible potential-dependent structural changes of the Co_3O_4 deposit. The displayed images were selected from a continuous series, recorded at the (404) Bragg peak during a CV in 0.1 M NaOH at 10 mV/s. They are shown after conversion to in-plane (q_{\parallel}) and out-of-plane (q_{\perp}) positions in reciprocal space, with the small black crosses marking the current and the large white crosses the initial peak position. By quantitative fits of peak position and width in both directions, $\varepsilon_{\perp,\parallel}$ and $d_{\perp,\parallel}$ were determined.

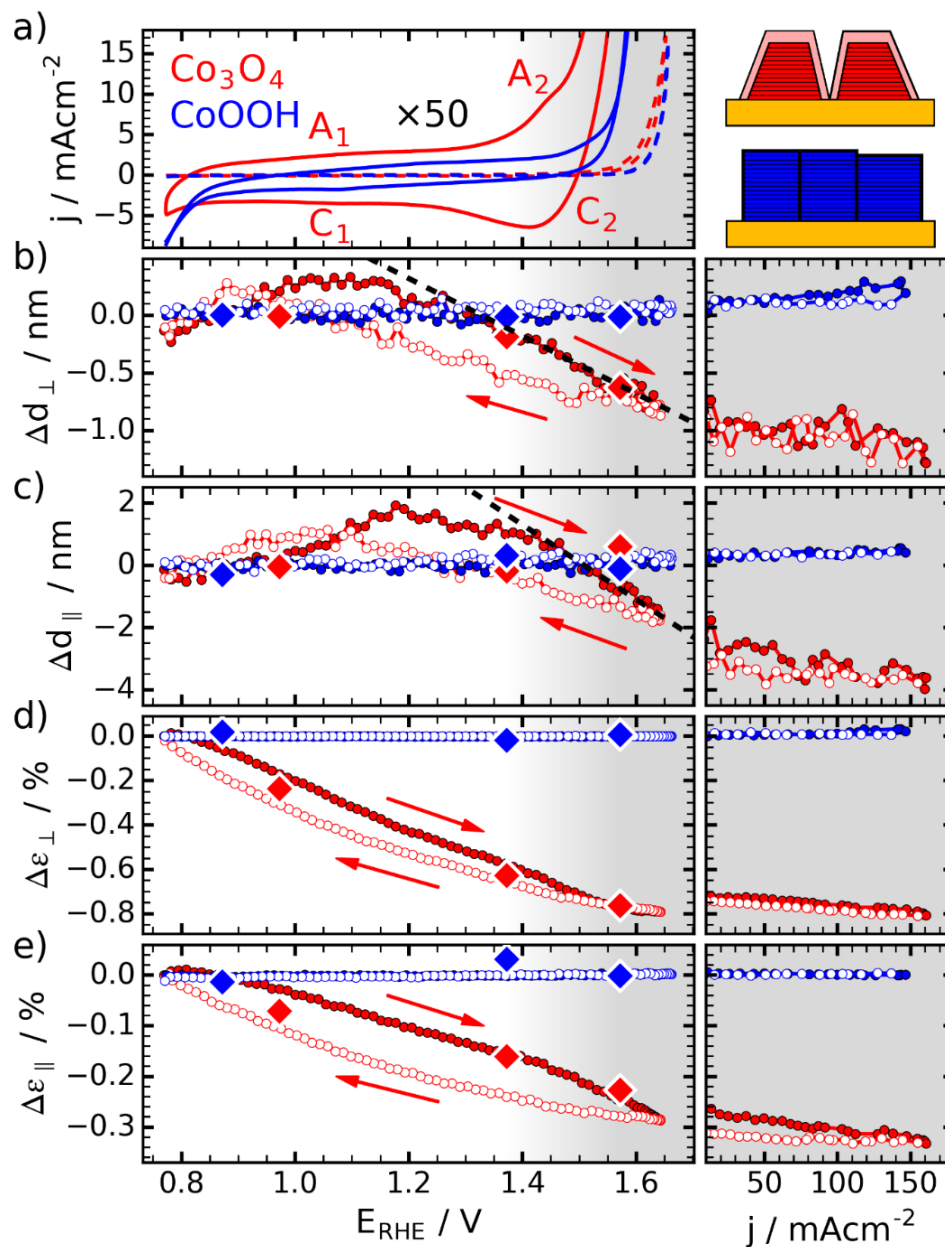


Figure 4: (a) CV and (b-e) *operando* SXR structural data for Co₃O₄/Au(111) (red) and CoOOH/Au(111) (blue), recorded simultaneously in 0.1 M NaOH at 10 mV/s. Presented are the potential-dependent changes in out-of-plane and in-plane (b,c) grain size $\Delta d_{\perp,\parallel}$ and (d,e) strain $\Delta \varepsilon_{\perp,\parallel}$ relative to the values at the lower potential limit. The right hand panel in (b-e) show the variations of these structural parameters as a function of OER current, obtained in a similar experiment. In all panels, filled and open symbols refer to the positive and negative going potential sweep, respectively. In addition, results of the structure under steady-state conditions are included for comparison (diamonds) and a schematic illustration of the film morphologies is included (upper right corner). All current densities j are given with respect to the geometric surface area of the Au(111) single crystal.

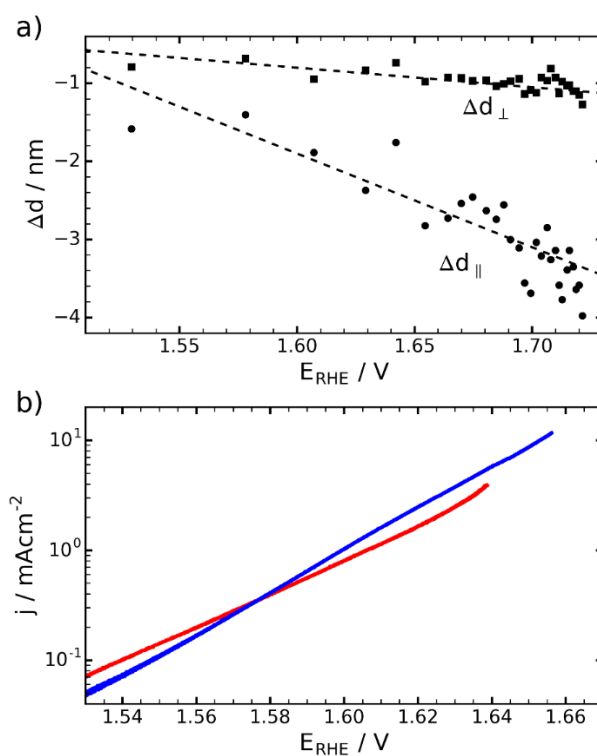


Figure 5: (a) Potential-dependent changes of the out-of-plane and in-plane grain size $\Delta d_{\perp,\parallel}$ of $\text{Co}_3\text{O}_4/\text{Au}(111)$ in the OER regime. (b) iR-corrected Tafel plots of $\text{CoOOH}(001)$ (blue) and $\text{Co}_3\text{O}_4(111)$ (red) films, recorded on the structurally characterized samples in the SXRD cell. The current density is given with respect to ECSA, accounting for the roughness factor ~ 1 and ~ 3 , respectively for $\text{CoOOH}(001)$ and $\text{Co}_3\text{O}_4(111)$ layers.

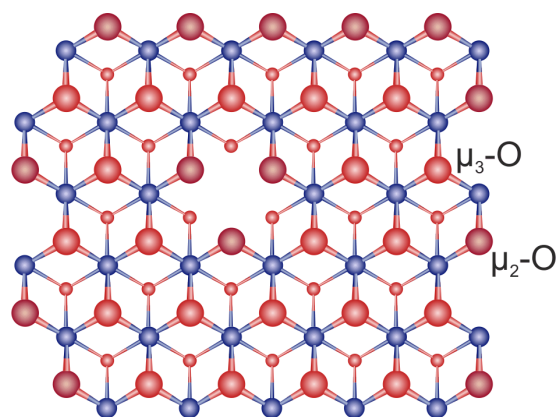


Figure 6: Atomic model (top view) of the topmost plane of the CoOOH(001) surface. Oxygen atoms are red and cobalt blue. O atoms on the ideal surface are threefold coordinated (μ_3 -O sites), whereas at steps and next to Co vacancies μ_2 -O sites (dark red) are found.

Table of content figure

